

This item is the archived peer-reviewed author-version of:

Optimal experiment design for element specific atom counting using multiple annular dark field scanning transmission electron microscopy detectors

Reference:

Sentürk Duygu Gizem, de Backer Annick, Friedrich Thomas, Van Aert Sandra.- Optimal experiment design for element specific atom counting using multiple annular dark field scanning transmission electron microscopy detectors
Ultramicroscopy - ISSN 1879-2723 - 242(2022), 113626
Full text (Publisher's DOI): <https://doi.org/10.1016/J.ULTRAMIC.2022.113626>
To cite this reference: <https://hdl.handle.net/10067/1909250151162165141>

Optimal experiment design for element specific atom counting using multiple annular dark field scanning transmission electron microscopy detectors

D.G. Sentürk^{a,b,*}, A. De Backer^{a,b}, T. Friedrich^{a,b}, S. Van Aert^{a,b}

^a*Electron Microscopy for Materials Science (EMAT), University of Antwerp, Groenenborgerlaan 171, 2020 Antwerp, Belgium*

^b*NANOLab Center of Excellence, University of Antwerp, Groenenborgerlaan 171, 2020 Antwerp, Belgium*

Abstract

This paper investigates the possible benefits for counting atoms of different chemical nature when analysing multiple 2D scanning transmission electron microscopy (STEM) images resulting from independent annular dark field (ADF) detector regimes. To reach this goal, the principles of statistical detection theory are used to quantify the probability of error when determining the number of atoms in atomic columns consisting of multiple types of elements. In order to apply this theory, atom-counting is formulated as a statistical hypothesis test, where each hypothesis corresponds to a specific number of atoms of each atom type in an atomic column. The probability of error, which is limited by the unavoidable presence of electron counting noise, can then be computed from scattering-cross sections extracted from multiple ADF STEM images. Minimisation of the probability of error as a function of the inner and outer angles of a specified number of independent ADF collection regimes results in optimal experimental designs. Based on simulations of spherical Au@Ag and Au@Pt core-shell nanoparticles, we investigate how the combination of two non-overlapping detector regimes helps to improve the probability of error when unscrambling two types of atoms. In particular, the combination of a narrow low angle ADF detector with a detector formed by the remaining annular collection regime is found to be optimal. The benefit is more significant if the atomic number Z difference becomes larger. In addition, we show the benefit of subdividing the detector regime into three collection areas for heterogeneous nanostructures based on a structure consisting of three types of elements, e.g., a mixture of Au, Ag and Al atoms. Finally, these results are compared with the probability of error resulting when one would ultimately use a pixelated 4D STEM detector and how this could help to further reduce the incident electron dose.

1. Introduction

The aberration-corrected electron microscope has become a powerful tool for the characterisation of complex nanostructures as it enables the acquisition of two-dimensional atomic resolution images of a sample under investigation [1]. High angle annular dark field scanning transmission electron microscopy (HAADF STEM) arises as one of the favourable imaging modes because of the direct interpretation of the image contrast in terms of chemical composition and thickness [2]. In addition to a visual interpretation, the availability of high precision measurements of the materials' structure parameters is another crucial factor for a better understanding of the structure-property relationship. This requires advanced quantitative analyses for which a statistical parameter estimation framework can be used [3–6]. Over the past years, many quantification procedures have been developed to determine thickness or composition from HAADF STEM images [7–9]. For the interpretation of the image intensities, many of these methods make use of the so-called scattering cross-section, which corresponds to the total intensity of scattered electrons by an atomic column [10, 11]. The scattering cross-section is a useful parameter for the quantitative interpretation of HAADF STEM images as it is sensitive to the number of atoms and the atom type while it

is robust to experimental parameters such as small sample mis-tilts, defocus, lens aberrations and source coherence [12, 13].

In many applications within the statistical parameter estimation framework, either the number of atoms in homogeneous nanostructures [14–16] or the chemical composition of heterogeneous structures with known or constant thickness were determined [17, 18]. To extend the atom-counting methodology to heterogeneous nanoparticles, one needs additional information to unscramble both the type and number of atoms. It was shown by van den Bos et al. [19] that prior knowledge concerning the shape of a core-shell nanoparticle can help to determine both the chemical composition and the number of atoms in a Ag-coated Au nanoparticle. However, prior knowledge will not always be available and the question is then whether it would be possible to characterise heteronanostructures without using any prior knowledge?

For this purpose, multimode atomic resolution annular dark field (ADF) STEM might be a solution during which STEM images are acquired from different detector regions [20]. The recent development of pixelated detectors provides a great flexibility here, since it enables the reconstruction of multiple conventional STEM images from several arbitrary detector regimes with varying inner and outer angles, without the need for pre-configured fixed detector angles [21–25]. Indeed, with a pixelated detector, for each probe position the two dimensional convergent beam electron diffraction pattern is recorded resulting

*sandra.vanaert@uantwerpen.be

in a 4D dataset. By applying annular detector masks to the 2D diffraction patterns, multiple STEM images can be extracted simultaneously from the 4D dataset. Such a multimode approach is dose-efficient and has been proven to be useful to retrieve different materials' properties simultaneously [25–28].

Before quantifying any structure parameters from multiple annular detector geometries, deriving the optimal detector design can significantly improve the precision with which the structure parameters can be determined. In the present work, we will derive optimal multiple angular detector regimes for which the number and type of atoms can be estimated with the highest precision. For this purpose, we will use the principles of statistical detection theory [5, 29, 30] to quantify the probability of error when unscrambling the type and number of atoms in mixed columns. The probability of error will be computed for the scattering cross-sections extracted from multiple ADF STEM images. The optimal inner and outer angles of a specified number of independent ADF collection regimes will be derived by minimising this probability of error as a function of the detector angles. The probability of error of the optimal detector settings will be compared with the probability of error that one could ultimately obtain by analysing the full dark field region of the 4D STEM dataset.

The organisation of the paper is as follows. In section 2, detection theory and the probability of error are discussed for the scattering cross-section from a single detector, scattering cross-sections from multiple detectors, and for the full dark field region of the 4D dataset. In section 3, an overview is given of the investigated cases to unscramble the number and type of atoms. Next, the results of the probability of error study will be presented for these different cases in section 4. Finally, in section 5, the results are further discussed and a conclusion is drawn.

2. Statistical detection theory

In this section, statistical detection theory will be introduced in order to quantify the probability to miscount the number of atoms, to misidentify the type of atoms, and/or to misidentify the 3D arrangement of atoms in a column. In this theory, the studied problem is formulated as a statistical hypothesis test, where each hypothesis corresponds to a possible outcome. In our study, we want to differentiate between multiple hypotheses corresponding to different numbers of atoms and column compositions. The total number of hypotheses is denoted as M and therefore we want to decide among M possible hypotheses:

$$\{\mathcal{H}_0, \mathcal{H}_1, \dots, \mathcal{H}_{M-1}\}. \quad (1)$$

The goal is now to quantify the probability of assigning the wrong hypothesis, i.e. the probability of error, which is described by the following formula in a Bayesian approach:

$$P_e = \sum_{i=0}^{M-1} \sum_{j=0}^{M-1} C_{ij} P(\mathcal{H}_i | \mathcal{H}_j) P(\mathcal{H}_i), \quad (2)$$

where

$$C_{ij} = \begin{cases} 1 & i \neq j \\ 0 & i = j \end{cases} \quad (3)$$

and where $P(\mathcal{H}_i | \mathcal{H}_j)$ is the conditional probability of deciding \mathcal{H}_i when \mathcal{H}_j is true. In this manner, all possible errors are weighted appropriately to yield an overall error measure. Decision rules are defined such that this probability of error is minimised. When assuming equal prior probabilities for each hypothesis, $P(\mathcal{H}_i) = 1/M$, it is shown that we should decide \mathcal{H}_k if

$$p(w; \mathcal{H}_k) > p(w; \mathcal{H}_i) \quad \forall i \neq k. \quad (4)$$

In this expression $p(w; \mathcal{H}_i)$ is the conditional probability function assuming \mathcal{H}_i to be true evaluated for the observation w_i . The exact expression for the probability functions will be discussed for the three different measures that will be used as a criterion to count the number of atoms and identify the type of atoms in a projected atomic column: scattering cross-section from a single ADF detector, scattering cross-sections from multiple independent ADF detectors, and the dark field region of a 4D STEM dataset. The three different measures are visualised in Fig. 1.

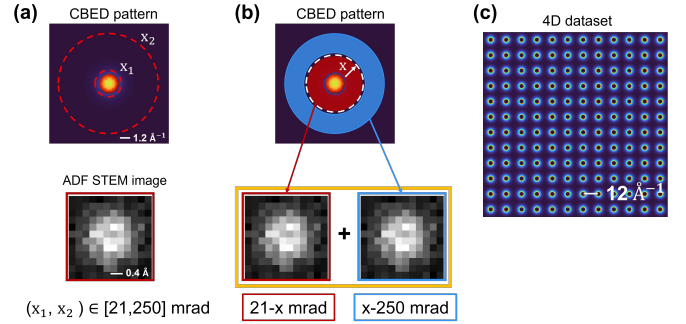


Figure 1: Three different measures (a) scattering cross-section from a single annular detector with varying inner or outer angle up to a maximum of 250 mrad (b) two scattering cross-sections from two independent non-overlapping detectors; the inner angle of the first detector and the outer angle of the second detector are fixed at 21 mrad and 250 mrad respectively and the common angle between the two detectors is varied, (c) the full dark field of the 4D dataset.

2.1. Scattering cross-section from a single ADF detector

The stochastic variable that describes the scattering cross-section from a single ADF detector is denoted as:

$$w^{CS} = \sum_{k=1}^K \sum_{l=1}^L \left[\sum_{m=1}^M \sum_{n=1}^N w_{klmn} \cdot D_{mn} \right] \cdot dx^2 \quad (5)$$

where w_{klmn} corresponds to the random variables describing the pixel intensities of the 4D dataset for a finite incident electron dose. The index kl denotes the probe position $(x_k, y_l)^T$ for a set of KL probe positions, the index mn refers to the pixel position in reciprocal space $(g_m^x, g_n^y)^T$ for a set of MN pixels, and dx denotes the real space pixel size. Furthermore, D_{mn} represents an annular detector function that is applied to each 2D CBED pattern in order to extract a 2D STEM image from the 4D dataset. This annular detector function D_{mn} is given by:

$$D_{mn} = \begin{cases} 1, & \text{if } m, n \in [R_{in}, R_{out}] \text{ of the annular detector} \\ 0, & \text{otherwise.} \end{cases} \quad (6)$$

R_{in} and R_{out} denote the inner and outer angle of the annular detector, respectively. When assuming that the pixels in a 4D STEM dataset are statistically independent electron counting results, the observations will be modelled as a Poisson distribution. Since a sum of independent Poisson distributed variables is known to be Poisson distributed, the pixel values in the STEM image will be Poisson distributed as well [31], and the variable

$$\sum_{k=1}^K \sum_{l=1}^L \left[\sum_{m=1}^M \sum_{n=1}^N w_{klmn} \cdot D_{mn} \right] \quad (7)$$

is therefore also Poisson distributed. The expected scattering cross-section value equals:

$$\mathbb{E}_{\mathcal{H}_i}[w^{CS}] = \sum_{k=1}^K \sum_{l=1}^L \left[\sum_{m=1}^M \sum_{n=1}^N \lambda_{\mathcal{H}_i,klmn} \cdot D_{mn} \right] \cdot dx^2 \quad (8)$$

$$= \sum_{k=1}^K \sum_{l=1}^L \lambda_{\mathcal{H}_i,kl} \cdot dx^2 \quad (9)$$

$$= \lambda_{\mathcal{H}_i} \cdot dx^2 \quad (10)$$

where $\lambda_{\mathcal{H}_i,klmn}$ is the expectation value for the pixel values of the 4D dataset, $\lambda_{\mathcal{H}_i,kl}$ denotes the expectation value for the STEM image pixel intensity at the probe position $(x_k, y_l)^T$, and the expectation value of the sum over the real space pixel values is denoted by $\lambda_{\mathcal{H}_i}$. Since this expectation will depend on which hypothesis \mathcal{H}_i is assumed to be true, also the probability function will depend on \mathcal{H}_i . These expectation values can be derived from a simulated 4D dataset for a given atomic structure and set of microscope parameters including a finite incident electron dose [32].

Since the multiplication of a Poisson distributed variable with a constant is no longer Poisson distributed, the conditional probability distribution for a scattering cross-section taking into account the constant factor dx^2 , is then given by

$$p(\omega^{CS}; \mathcal{H}_i) = \frac{(\lambda_{\mathcal{H}_i})^{\omega^{CS}/dx^2}}{\left(\frac{\omega^{CS}}{dx^2}\right)!} \exp(-\lambda_{\mathcal{H}_i}). \quad (11)$$

This probability function describes the probability that the observation w^{CS} is equal to ω^{CS} . From this expression for the conditional probability function and Eq. (2), the probability of error can be computed analytically for the scattering cross-section from a single ADF detector from the overlapping areas of the conditional probability functions under the different hypotheses. For overlapping areas, a wrong decision is made based on the decision rule of Eq.(4), thus corresponding to the probability of error. Details on the computation of the probability of error for the scattering cross-section from a single ADF detector are provided by De Backer et al. [30].

2.2. Scattering cross-sections from multiple independent ADF detectors

Analogous to the definition of the stochastic variable for the scattering cross-section from a single ADF detector, the

stochastic variable for scattering cross-sections from multiple independent ADF detectors can be defined. For simplicity, the formulas will be introduced for two independent ADF detectors, but can effortlessly be extended to multiple independent ADF detectors. For two independent ADF detectors, the stochastic variable is described by:

$$\mathbf{w}_{\text{mult.det}}^{CS} = [w_{D^1}^{CS}, w_{D^2}^{CS}]^T \quad (12)$$

where $w_{D^j}^{CS}$ is the stochastic variable for the scattering cross-section of a specific annular detector function j :

$$w_{D^j}^{CS} = \sum_{k=1}^K \sum_{l=1}^L \left[\sum_{m=1}^M \sum_{n=1}^N w_{klmn} \cdot D_{mn}^j \right] \cdot dx^2. \quad (13)$$

For $j = 1$ and $j = 2$, independent annular detector regions are selected with the annular detector function D_{mn}^j . In case of multiple scattering cross-section values retrieved from different non-overlapping detectors, the conditional joint probability function is given by

$$p(\omega_{\text{mult.det}}^{CS}; \mathcal{H}_i) = \prod_{j=1}^2 \frac{(\lambda_{\mathcal{H}_i, D^j})^{\omega_{D^j}^{CS}/dx^2}}{\left(\frac{\omega_{D^j}^{CS}}{dx^2}\right)!} \exp(-\lambda_{\mathcal{H}_i, D^j}) \quad (14)$$

where $\lambda_{\mathcal{H}_i, D^j}$ indicates the expectation value of the sum over the real space pixel values for detector D^j .

Since we have a *joint* probability function, which is highly multidimensional, for the stochastic variable $\mathbf{w}_{\text{mult.det}}^{CS}$ for multiple scattering cross-section values, it is not possible to simply, analytically, compute the probability of error from the overlapping areas of the conditional joint probability functions. In this case, the probability of error can only be computed using multiple noise realisations under the different hypotheses. The expectation values for the scattering cross-sections corresponding to the two independent detector regimes are extracted from detailed simulated 4D datasets under the different hypotheses. Next, for each hypothesis, 1000 Poisson distributed observations $\mathbf{w}_{\text{mult.det}}^{CS}$ were generated following the joint probability function given by Eq.(14). For every noise realisation, hypothesis \mathcal{H}_k is decided following the decision rule given by Eq.(4). From the fraction of wrong assignments, the probability of error can then be computed.

2.3. Dark field region of a 4D STEM dataset

As a third measure to evaluate the probability of error for counting atoms of different types, we introduce the full dark field region of a 4D STEM dataset. Only the dark field region of the 4D dataset is utilised in order to obtain a fair comparison with the scattering cross-sections which are also only extracted from the dark field detector regions, i.e. the inner angle of the annular detector is larger than the probe convergence angle. In this case, the stochastic variable can be described by:

$$\mathbf{w}^{4D} = [w_{1,1,1,1}, w_{1,1,1,2}, w_{1,1,2,1}, w_{1,2,1,1}, w_{2,1,1,1}, \dots, w_{K,L,M',N'}]^T \quad (15)$$

where $w_{klm'n'}$ corresponds to the random variables describing the pixel intensities of the full dark field region of the 4D dataset. Important to note here is that the ‘primes’ on the indices n' and m' indicate that in the CBED pattern only the pixel values corresponding to the dark field region are selected as compared to w_{klmn} introduced in Eq.(5) where m and n correspond to all pixels of the CBED pattern. The conditional joint probability function for the dark field region of the 4D STEM dataset can be expressed as

$$p(\omega^{4D}) = \prod_{k=1}^K \prod_{l=1}^L \prod_{m'=1}^{M'} \prod_{n'=1}^{N'} \frac{(\lambda_{klm'n'})^{\omega_{klm'n'}}}{\omega_{klm'n'}!} \exp(-\lambda_{klm'n'}). \quad (16)$$

In this expression $\lambda_{klm'n'}$ corresponds to the expectation values for the pixel intensities in the dark field region of the 4D STEM dataset. Also for the dark field region of the full 4D dataset, we have a *joint* probability function and we will generate noise realisations under the different hypotheses to compute the probability of error. For this purpose here, and due to the large 4D STEM dataset, for each hypothesis, 10 Poisson distributed observations are generated following the joint probability function given by Eq.(16).

3. Simulation settings

An elaborate simulation study is performed for five different case studies in order to investigate the probability of error defined in Section 2. For this purpose, simulations of 4D datasets are performed for:

- (a) 40 hypotheses: pure Ag (Z=47) and Au (Z=79) atomic columns up to 20 atom thick columns
- (b) 20 hypotheses: different depth locations of a single Au (Z=79) atom in a 20 atom thick Ag (Z=47) column
- (c) 190 hypotheses: mixed atomic columns containing both Ag (Z=47) and Au (Z=79) atoms with compositions that can be expected for a Au@Ag core-shell nanoparticle up to 20 atoms thickness
- (d) 190 hypotheses: mixed atomic columns containing both Pt (Z=78) and Au (Z=79) atoms with compositions that can be expected for a Au@Pt core-shell nanoparticle up to 20 atoms thickness
- (e) 990 hypotheses: mixed atomic columns containing Au (Z=79), Ag (Z=47), and Al (Z=13) atoms with compositions that can be expected for a layered Al-Ag-Au structure up to 20 atoms thickness

These five case studies are visualised in Fig. 2. For each hypothesis a full 4D dataset has been simulated with the MULTEM software [32] using frozen phonon simulations for an aberration corrected microscope. It should be noted that inelastic plasmon excitations are not included in the simulations. These contributions will be important for quantitatively matching simulated and experimental intensity values at low scattering angles [33]. The simulations are performed for a crystal with thickness and

composition defined by each hypothesis. The simulation settings are listed in Table 1. In order to use realistic Debye-Waller B factors for the Au-Ag and Au-Pt mixed columns, molecular dynamics simulations were carried out at room temperature using LAMMPS assuming core-shell nanoparticles [34, 35]. From these simulations, the mean squared displacements are computed. The Debye-Waller B factor is then given by:

$$B = \frac{8}{3} \pi^2 \langle u^2 \rangle \quad (17)$$

where $\langle u^2 \rangle$ is the mean squared displacement of an atom. The atomic interactions were modelled using the EAM potentials for Au, Ag, and Pt [36]. For the layered structure containing three types of elements, the Debye-Waller B factors for bulk materials at room temperature are used.

The probability of error is computed for the three different measures introduced in Section 2. For the scattering cross-sections measurements, we evaluate and optimise the inner and outer radii of a single and multiple annular STEM detectors in terms of quantitatively determining the number and type of atoms in an atomic column. The probability of error obtained for the scattering cross-sections extracted from the optimal single or two independent ADF detectors is also compared to the probability of error that we would obtain when ultimately utilising the full dark field region of the 4D dataset. When optimising two independent annular detectors, the inner angle of the first detector and the outer angle of the second detector are kept fixed at 21 mrad and 250 mrad respectively. The probability of error is then computed as a function of a common angle x . For the fifth case study, considering three different types of elements, the possibility of subdividing the detector into more than two independent detectors is investigated as well. In this case, the first detector has a fixed inner angle of 21 mrad and varying outer angle, the middle detector has both a varying inner and outer detector angle, and the third detector has a fixed outer angle of 250 mrad and a varying inner angle. The minimal angular thickness of the middle detector is 2 mrad.

The actual numbers of the probability of error do not only depend on the inner and outer annular detector angles but also on the incident electron dose. Once the optimal design has been derived, one can investigate the lowest possible incident electron dose for which the probability of error reaches an acceptable value. Therefore, the probability of error will be computed as a function of the incident electron dose for the three different measures, using the optimal inner and outer detector angles for the scattering cross-sections and for the full dark field region of the 4D dataset.

4. Optimal experiment design to unscramble type and number of atoms

4.1. Pure Au and Ag atomic columns

Before investigating the optimal experiment design of mixed atomic columns, the probability of error was calculated in order to distinguish between both the number and type of atoms for pure Au and Ag atomic columns up to 20 atoms thickness.

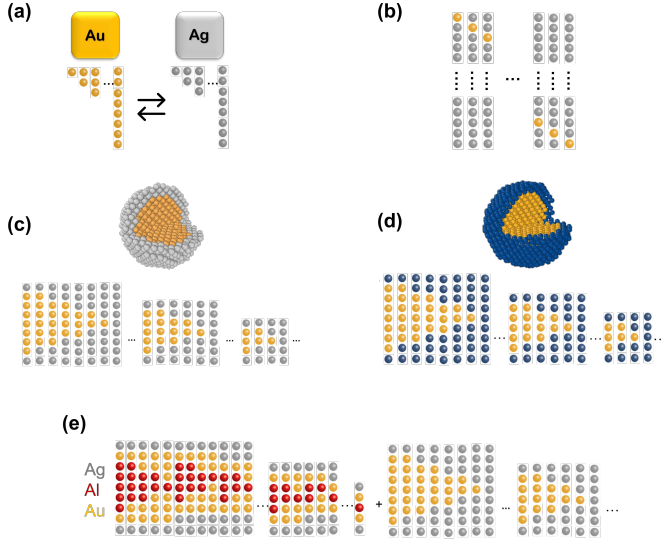


Figure 2: Illustration of the five case studies: (a) pure Au and Ag atomic columns with varying thickness from 1 up to 20 atoms, (b) depth location of a single Au impurity atom in a 20 atom thick column, (c) Au@Ag core-shell nanoparticle compositions for 3 up to 20 atoms thick columns, (d) Au@Pt core-shell nanoparticle compositions for 3 up to 20 atoms thick columns, and (e) Au-Ag-Al core-shell compositions for 5 up to 20 atoms thick columns.

Different types of elements will result in a different scattering distribution in the CBED patterns. Indeed, it is expected that the scattering cross-section of a thicker Ag column coincides with that of a thinner Au column complicating atom-counting as compared to having only atomic columns of one type. In Fig. 3(a) the results of the probability of error for the scattering cross-sections resulting from a single or 2 independent detectors are presented for an incident electron dose of $10^4 e^-/\text{\AA}^2$. When using the scattering cross-section from a single detector, the suggested optimal angles are 31-250 mrad corresponding to a probability of error of 12%. When using the scattering cross-sections from two independent detectors, the probability of error can be reduced significantly to almost zero percent. The suggested optimal combination of independent detector rings is given by 21-43 mrad and 43-250 mrad.

The probability of error is evaluated as a function of the incident electron dose in Fig. 3(b) for the three different measures introduced in Section 2. As expected, the probability of error decreases for an increasing electron dose for the three curves. If a maximum probability of error of 5% would be taken as acceptable, the required incident electron dose would be $4 \cdot 10^4 e^-/\text{\AA}^2$ when using a single optimal ADF detector. This incident electron dose can be further reduced to $5 \cdot 10^3 e^-/\text{\AA}^2$ based on the scattering cross-sections of the optimal two independent annular detectors and to $10^3 e^-/\text{\AA}^2$ when exploring the full dark field region of the 4D STEM dataset. These results clearly show the potential benefit of analysing multiple 2D STEM images when counting atoms in mixed columns.

In order to better understand the suggested optimal detector settings and how the combination of scattering cross-sections from

Parameter	Value
Zone orientation	[110]
Acceleration voltage	300 kV
Defocus	-17.184 Å
Spherical aberration	0.001 mm
Semi-convergence angle	20 mrad
Real space probe sampling distance	0.2 Å
Number of pixels in real space ($K \times L$)	15 × 21
Pixel size in reciprocal space	0.02 Å ⁻¹
Number of pixels in reciprocal space ($M \times N$)	1400 × 1400
Maximal outer detector angle	276 mrad
Slice thickness	1.44 Å
Incident electron dose	$10^4 e^-/\text{\AA}^2$
Debye-Waller B factor Au bulk	0.625 Å ²
Debye-Waller B factor Ag bulk	0.762 Å ²
Debye-Waller B factor Al bulk	0.833 Å ²
Debye-Waller B factor Au in Au@Ag NP	1.248 Å ²
Debye-Waller B factor Ag in Au@Ag NP	1.870 Å ²
Debye-Waller B factor Au in Au@Pt NP	1.324 Å ²
Debye-Waller B factor Pt in Au@Pt NP	1.826 Å ²

Table 1: Settings used for multislice simulations with MULTTEM software.

a low angle ADF detector and medium angle ADF detector reduce the probability of error, the scattering cross-sections and their probability distribution functions are highly informative. The probability functions for the 40 hypotheses of the pure Ag and Au atomic columns are shown in Fig. 4(a) for the optimal single detector of 31-250 mrad under an incident electron dose of $10^4 e^-/\text{\AA}^2$. For both Au and Ag, there is a monotonic increase for the scattering cross-sections. However, a significant amount of probability functions is overlapping preventing to identify the correct type and number of atoms for these hypotheses. Using two independent detectors, from which scattering cross-sections can be determined, results in a more unique relation between the measurements, i.e. the combination of two scattering cross-section values and the hypotheses in the study. In order to visualise the removal of many of the overlapping hypotheses, a scatter plot is constructed in which the scattering cross-sections of the second detector are plotted as a function of the scattering cross-sections of the first detector. For most combinations of scattering cross-section values a unique value is observed. It is important to note that we still have to take into account the finite overlap of the probability functions which is also visualised in this figure. Even then, most of the cases are well-separated if the electron dose is sufficiently large, whereas for scattering cross-sections from a single detector, many of the Ag atomic columns do (completely) overlap with the thinner Au atomic columns.

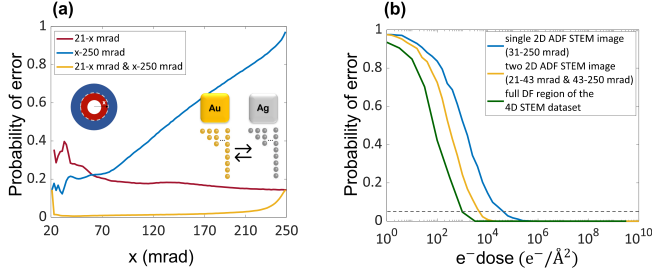


Figure 3: **Pure Ag and Au columns** - (a) Probability of error as a function of the outer angle of a single ADF detector with fixed inner angle (red), the inner angle of a single ADF detector with a fixed outer angle (blue), and the common angle x for two independent detectors (yellow) for an incident electron dose of $10^4 e^-/\text{\AA}^2$ (b) Probability of error as a function of the incident electron dose calculated for the optimal single ADF detector (blue), the optimal two independent ADF detectors (yellow), and for the full dark field region of the 4D STEM dataset (green).

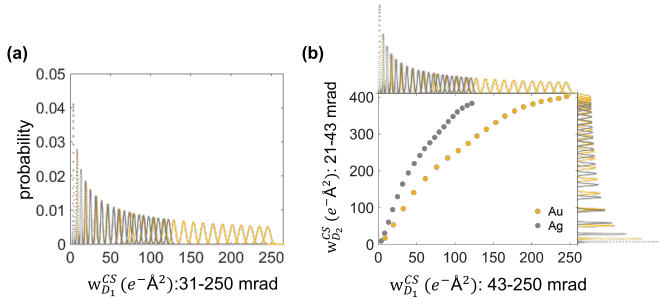


Figure 4: **Pure Ag and Au columns** - (a) Probability functions for the pure Au and Ag atomic columns for a single detector ranging from 31-250 mrad. (b) Scatter plot of the scattering cross-sections from the optimal two independent detectors ($D_1 = 43-250 \text{ mrad}$ and $D_2 = 21-43 \text{ mrad}$) for an incident electron dose of $10^4 e^-/\text{\AA}^2$ illustrating the increased uniqueness as compared to the scattering cross-sections of a single detector. To illustrate the overlap, the probability functions are also plotted on the top and right axes.

4.2. Depth location of a single Au impurity atom

Subsequently, the research problem is extended to heterogeneous atomic columns. As a first step, the possibilities and limitations to derive the depth location of a single Au impurity atom in a 20 atoms thick Ag atomic column is investigated. In this case, each hypothesis corresponds to one of 20 possible depth locations of the Au atom which is illustrated in Fig. 2(b). It has been shown by van den Bos et al. [37] that the scattering cross-sections are sensitive to the depth location of a single impurity atom. However, the required incident electron dose is too high to avoid beam damage during the experimental acquisition. Here, we investigate the possible benefit of using scattering cross-sections resulting from the combination of two independent detectors. Similar to the results in section 4.1, we evaluate the probability of error as a function of the shared common angle x of two independent detectors and the inner and outer angle of the single detectors, under an incident electron dose of $10^4 e^-/\text{\AA}^2$. The results are displayed in Fig. 5(a). Under this incident electron dose, the combination

of two detectors (yellow curve) does not reduce the probability of error significantly. Nevertheless, the optimal angles can still be determined from this analysis. For the scattering cross-section from a single ADF detector, the minimal probability of error is observed for 31-250 mrad and for the combination of two scattering cross-sections from the independent detectors, the suggested optimal angles are 21-31 mrad and 31-250 mrad. When evaluating the probability of error as a function of the incident electron dose, shown in Fig. 5(b), the benefit of two independent detector rings is clearly present at higher doses for quantifying the depth location of a single Au impurity atom. For example, under an incident electron dose of $10^6 e^-/\text{\AA}^2$, the probability of error decreases from 30% to only 5%. Besides, the green curve in Fig. 5(b) illustrates that to obtain a probability of error of 5%, the required incident electron dose can be further reduced to $3 \cdot 10^4 e^-/\text{\AA}^2$ if the dark field region of the full 4D dataset can be employed. This observation makes the 4D dataset a promising tool to extract the depth location under more realistic incident electron doses.

The suggested optimal detector settings derived from Fig. 5, can be understood in a similar manner as the previous case for the two types of pure atomic columns. In Fig. 6(a) and (b), scattering cross-sections are shown for the optimal detector regimes ranging from 31-250 mrad and 21-31 mrad for an incident electron dose of $10^6 e^-/\text{\AA}^2$. The single Au impurity atom is moved from the top to the bottom of the Ag atomic column. Despite the small variation in scattering cross-section value with depth location, the different trends for those two detector regimes suggest that the distinction of the different hypotheses is simplified with the introduction of the second detector. This is further confirmed by the scatter plot in Fig. 6(c), where the different hypotheses are not overlapping. However, when taking into account the finite incident electron dose, it is clear that some combinations of hypotheses remain indistinguishable, whereas other combinations clearly benefit from the presence of the second detector.

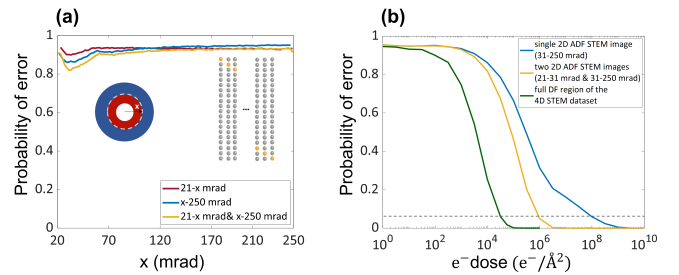


Figure 5: **Depth location of Au atom** - (a) Probability of error as a function of the outer angle of a single ADF detector with fixed inner angle (red), the inner angle of a single ADF detector with a fixed outer angle (blue), and the common angle x for two independent detectors (yellow) for an incident electron dose of $10^4 e^-/\text{\AA}^2$ (b) Probability of error as a function of the incident electron dose calculated for a single ADF detector (blue), two independent ADF detectors (yellow), and for the full dark field region of the 4D STEM dataset (green).

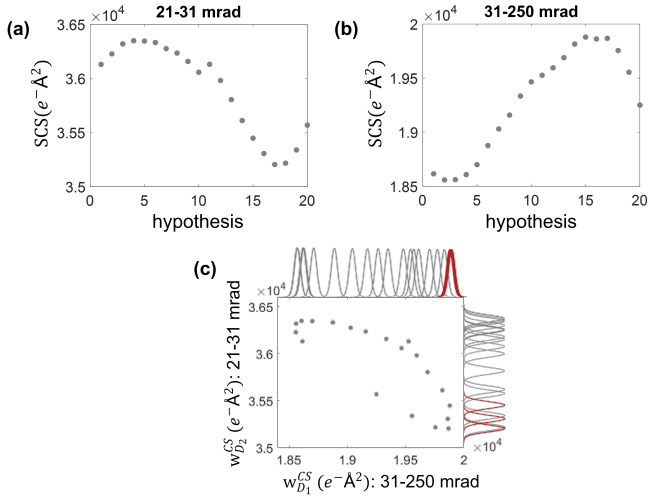


Figure 6: **Depth location of Au atom** - Scattering cross-sections as a function of the depth location of a single Au atom in a 20 atom thick Ag atomic column for (a) 21-31 mrad and (b) 31-250 mrad. (c) Scatter plot of the scattering cross-sections from the optimal two independent detectors ($D_1 = 31-250$ mrad and $D_2 = 21-31$ mrad) for an incident electron dose of $10^6 e^-/\text{\AA}^2$ illustrating the increased uniqueness as compared to the scattering cross-sections of a single detector. To illustrate the overlap, the probability functions are also plotted on the top and right axes. The curves highlighted in red illustrate the second detector helps to unscramble the hypotheses which are overlapping for the first detector.

4.3. Au@Ag core-shell nanoparticle

The possible benefit of analysing scattering cross-sections extracted from two independent detector regions were investigated for two exploratory case studies in the previous sections. Now, we will examine the advantage for a true heterogeneous system. For this purpose, we consider hypotheses corresponding to the atomic columns of a Au@Ag core-shell nanoparticle. For this type of structure, the total number of atoms and the number of Ag and Au atoms in the column varies. Since the combination of two non-overlapping detector signals does not provide any significant advantage to obtain the depth location of the specific atom types using an incident electron dose of $10^4 e^-/\text{\AA}^2$, we limited the number of hypotheses by assuming that the Au core is located at the centre of the structure. The thickness g of the atomic columns is varied from 1 up to 20 atoms. For a given thickness $g > 2$, the number of Au atoms of the core is varied from 0 up to $g - 2$ as illustrated in Fig. 2(c). In Fig. 7(a), the probability of error is evaluated as a function of the detector angles for an incident electron dose of $10^4 e^-/\text{\AA}^2$. The probability of error values that are obtained here are higher as compared to the first case in which the pure Ag and Au atomic columns were considered. This can be easily understood from the increased number of hypotheses and thus complexity of the studied problem. However, for the hypotheses corresponding to the core-shell structure, the advantage of using the scattering cross-sections from the detector pair is more pronounced. The probability of error can be reduced from 73% to 26% when the scattering cross-sections of the optimal combination of two independent ADF detectors are employed, rather

than the scattering cross-section from a single optimal ADF detector. The suggested optimal angles for a single detector equal 27-250 mrad, while 21-27 mrad and 27-250 mrad are found as the optimal angles for the detector pair. Fig. 8(b) illustrates that the required incident electron dose can be reduced by a factor of 10^2 to reach a probability of error as low as 5%. Even a factor of 10^3 can be gained for the incident electron dose, when the dark field region of the full 4D dataset is utilized. However, it is clear that the major improvement is introduced by the introduction of the second independent detector region.

Also here, we will illustrate how we can understand the benefit of using a second non-overlapping detector for unscrambling the number and type of atoms in a Au@Ag core-shell nanoparticle. Since we consider here 190 possible hypotheses, a simplified representation will be used. In Fig. 8(a) and (b), the scattering cross-section values are presented for the two independent detectors ($D_1 = 27-250$ mrad and $D_2 = 21-27$ mrad) for an incident electron dose of $10^4 e^-/\text{\AA}^2$. In Fig. 8(b), each decrease of dots corresponds to a decreasing Au/Ag ratio in the mixed atomic column for a constant thickness. The total thickness increases from 1 up to 20 from left to right in the figure. This means that, for a constant thickness, the composition of the mixed atomic columns can be distinguished from the scattering cross-sections of the ADF STEM images with a detector of 27-250 mrad. In Fig. 8(a), one can hardly identify the atomic columns with varying Au/Ag ratio. However, one can still observe a monotonic increase with thickness. Therefore, this thin annular detector can help to determine the thickness of mixed atomic columns of different thicknesses which have the same scattering cross-section values for the detector of 27-250 mrad. To clarify this, hypotheses are selected for atomic columns with varying thickness from 15 up to 20 atoms for which the scattering cross-sections are similar at the single optimal ADF detector ranging from 27-250 mrad. The selected hypotheses are indicated by arrows and the corresponding atomic columns are illustrated in the insets of Fig. 8(a) and (b). The probability functions corresponding to those hypotheses are shown in Fig. 8(c) and demonstrate that there is less overlap between the different hypotheses for the 21-27 mrad detector clearly indicating how this detector helps distinguishing the different hypotheses. Also for another selection of hypotheses, which are overlapping in one of the two detectors, the same reasoning can be used. This explains how the combination of two detectors significantly reduces the probability of error for characterising the mixed atomic columns in terms of number and type of atoms.

4.4. Au@Pt core-shell nanoparticle

From the analysis of the Au@Ag core-shell nanoparticle hypotheses, it is clear that the use of scattering cross-sections from two non-overlapping ADF detectors can be beneficial for unscrambling the number and type of atoms in mixed atomic columns. However, Ag and Au have significantly different atomic numbers ($Z_{\text{Ag}} = 47$ and $Z_{\text{Au}} = 79$). The question is now whether the combination of two independent detector signals can also help for mixed atomic columns with closer atomic numbers. To investigate this, the same hypotheses are considered corresponding to a spherical core-shell nanoparticle, where

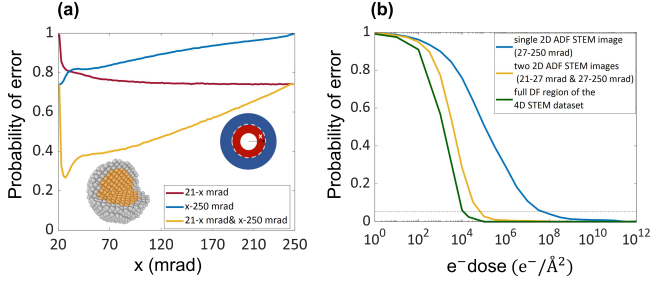


Figure 7: **Au@Ag** - (a) Probability of error as a function of the outer angle of a single ADF detector with fixed inner angle (red), the inner angle of a single ADF detector with fixed outer angle (blue), and the common angle x for two independent detectors (yellow) for an incident electron dose of $10^4 e^-/\text{\AA}^2$. (b) Probability of error as a function of the incident electron dose calculated for a single ADF detector (blue), two independent ADF detectors (yellow), and for the full dark field region of the 4D STEM dataset (green).

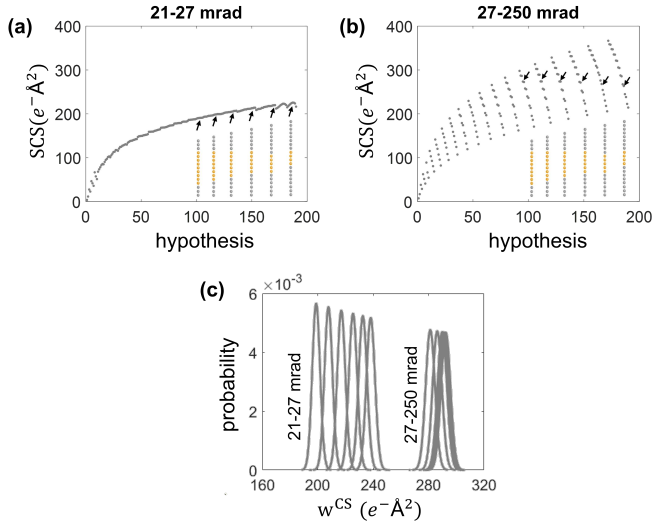


Figure 8: **Au@Ag** - Scattering cross-sections as a function of different compositions and thicknesses for Au@Ag mixed atomic columns for detectors ranging from (a) 21-27 mrad and (b) 27-250 mrad. (c) Probability functions for the selected hypotheses for an incident electron dose of $10^4 e^-/\text{\AA}^2$ based on the scattering cross-sections obtained from the two independent detectors.

the Ag atoms are now replaced by Pt atoms (see Fig. 2(d)). The difference in atomic number is then only 1.

In Fig. 9(a), the probability of error as a function of the detector angles is shown for an incident electron dose of $10^4 e^-/\text{\AA}^2$. Compared to the analysis for the Au@Ag core-shell nanoparticle and as expected, the probability of error is significantly larger. The optimal settings are found at 29-250 mrad for the scattering cross-section resulting from a single ADF detector. For the scattering cross-sections from the detector pair, the analysis suggests 21-29 mrad and 29-250 mrad as the optimal angles. In addition, a local minimum is found for 21-63 mrad and 63-250 mrad. The evaluation of the probability of error as a function of the incident electron dose shows that the required incident electron dose to reach a probability of error of the or-

der of 5%, can be reduced by a factor of 10 using two optimal non-overlapping detectors. The required incident electron dose can be further reduced by a factor of 10^3 when the dark field region of the full 4D dataset is used. This result is comparable to the probability of error analysis for determining the depth location of a single impurity atom described in 4.2. In both cases, the different hypotheses are difficult to distinguish because of the small differences in scattering cross-section values and the benefit of using two independent ADF detectors is only present when using higher incident electron doses.

The results here can be understood in a similar manner as for the Au@Ag example. Fig. 10(a) and (b) show the scattering cross-section values for the hypotheses of the mixed atomic columns under an incident electron dose of $10^6 e^-/\text{\AA}^2$. However, because of the closely separated atomic numbers of Pt and Au, the decrease in scattering cross-section with the decreased Au/Pt ratio for atomic columns of the same thickness is less pronounced as compared to the observed decrease for the Au@Ag atomic columns. The narrow detector, for which the scattering cross-sections are increasing for decreasing Au/Pt ratio, will now help to determine the composition of the atomic columns which have a similar scattering cross-section value in the detector with 29-250 mrad as detector angles. Fig. 10 shows the probability functions for a set of 3 selected hypotheses with a thickness of 20 atoms for both detectors. Although the second detector will help, the large amount of overlap between the probability functions, will limit the benefit as compared to the Au@Ag example in terms of the probability of error even for an incident dose of $10^6 e^-/\text{\AA}^2$.

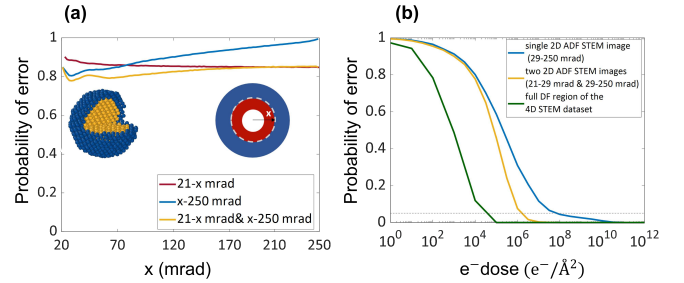


Figure 9: **Au@Pt** - (a) Probability of error as a function of the outer angle of a single ADF detector with fixed inner angle (red), the inner angle of a single ADF detector with fixed outer angle (blue), and the common angle x for two independent detectors (yellow) for an incident electron dose of $10^4 e^-/\text{\AA}^2$. (b) Probability of error as a function of the incident electron dose calculated for a single ADF detector (blue), two independent ADF detectors (yellow), and for the full dark field region of the 4D STEM dataset (green).

4.5. Al@Au@Ag trimetallic nanostructure

Next, the validity of using a combination of multiple detectors is assessed for the characterisation of multimetallic nanostructures since many technologically attractive materials consist of more than two types of elements [38, 39]. Here, a trimetallic nanostructure consisting of Au, Ag, and Al atoms is considered, where the atomic number of Al ($Z = 13$) is significantly

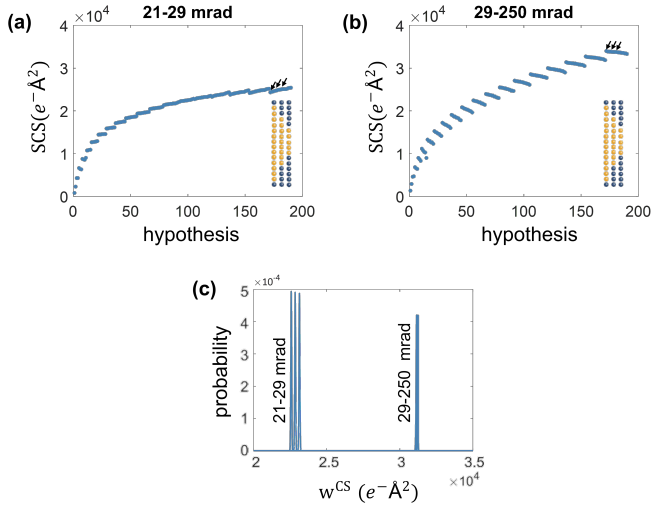


Figure 10: **Au@Pt** - Scattering cross-sections as a function of different compositions for Au@Pt mixed atomic columns with varying number of Au/Pt ratio for detectors ranging from (a) 21-29 mrad and (b) 29-250 mrad. (c) Probability functions for the selected hypotheses for an incident electron dose of $10^6 e^-/Å^2$ based on the scattering cross-sections obtained from the two independent detectors.

lower. For these mixed atomic columns, the possibility of deriving three independent detector regions is explored. For the hypotheses of the trimetallic structure, a complex layered structure is considered, i.e. Al as the central layer, Au as the middle layer, and Ag as the outer layer, as illustrated in Fig. 2(e). Also here the total thickness g is varied from 1 up to 20 atoms. Both bimetallic and trimetallic mixed atomic columns are included in the set of hypotheses. For the bimetallic atomic columns, the same set of hypotheses as in 4.3 is used. For the atomic columns with three types of elements with a thickness $g > 4$, the number of Al atoms is varied from 1 up to $g - 4$, and the number of Au atoms from 2 up to $g - 3$. This results in a total of 990 hypotheses. This illustrates also the increasing complexity of the possible combinations for multiple elements in the atomic columns. Because of the large number of hypotheses, only 100 noise realisations are considered for the computation of the probability of error for the multiple detectors.

As a first step, the detector region is subdivided into only two detectors to investigate its possible benefit for this trimetallic nanostructure. Fig. 11(a) shows that optimal settings for the combination of two detectors are found as 21-31 mrad and 31-250 mrad. As compared to the probability of error that is obtained for the scattering cross-section of a single detector, the introduction of a second detector reduces the probability of error already 30% with $10^4 e^-/Å^2$ as the incident electron dose. Since one of the two detectors of this optimal detector pair includes only a narrow detector ring of 10 mrad, we will further subdivide the detector of 31-250 mrad to explore whether the probability of error can be further reduced by subdividing the dark field region into three annular detectors. This result is also displayed in Fig. 11(a). The optimum is found for fractioning the detector into rings given by the following angles:

21-31 mrad, 31-35 mrad, and 35-250 mrad, reducing the probability of error further with 60%.

From the probability of error as a function of the incident electron dose, shown in Fig. 11(b), it is clear that the introduction of the second detector has the largest impact in reducing the dose. Nevertheless, a significant reduction in the required electron dose is observed with the subdivision into three detectors to reach a probability of error as low as 5%. The required electron dose can be further reduced when employing the full dark field region of the 4D STEM dataset. Due to the large amount of hypotheses, the probability of error has been computed for a limited number of incident doses in this case.

The subdivision of the detector into three annular detector regions introduces a significant reduction for the probability of error. A more extended analysis optimisation of the angles of the detectors might reduce the probability of error even further. However, such a full optimisation is computationally very expensive. To illustrate the advantage of the combination of three independent detectors, four hypotheses are selected for which the scattering cross-sections overlap in two of the three detectors as illustrated in Fig. 12 for an incident electron dose of $10^4 e^-/Å^2$. In this case, the independent information from the third detector helps further unscrambling the hypotheses in a similar manner as an extra detector helps for the bimetallic examples described in the previous sections. The selected hypotheses correspond to atomic columns with a thickness from 14 up to 17 atoms. The composition of the atomic columns only differs in the number of Al atoms, while the number of Au (3 atoms) and Ag (5 atoms) atoms is the same for the four hypotheses. The less overlapping probability functions of the selected hypotheses here implies that the 31-35 mrad thin annular detector is relatively more sensitive as compared to the other two annular detectors to distinguish the number of Al atoms when the Au/Ag ratio is constant in the atomic columns.

5. Discussion and conclusions

In this work, we applied the principles of detection theory to determine optimal multiple ADF STEM detector regions for quantifying the type and number of atoms in heterogeneous atomic columns. The analysis was performed for the scattering cross-sections that can be extracted from multiple ADF STEM images. By minimising the probability of error as a function of the detector angles of the multiple detector regions, the detector design could be optimised. For this purpose, simulated 4D STEM datasets are extensively used to simultaneously extract scattering cross-sections from different angular detector collection regimes. As a reference, the probability of error and optimal detector design is also computed for the scattering cross-section from a single ADF detector. In addition, we also computed the probability of error that is expected when using the full dark field region of the 4D dataset. This represents the minimal probability of error that one could obtain when one would ultimately be able to extract all the information from the full dark field region of the 4D dataset.

Within this paper, five different case studies were investigated.

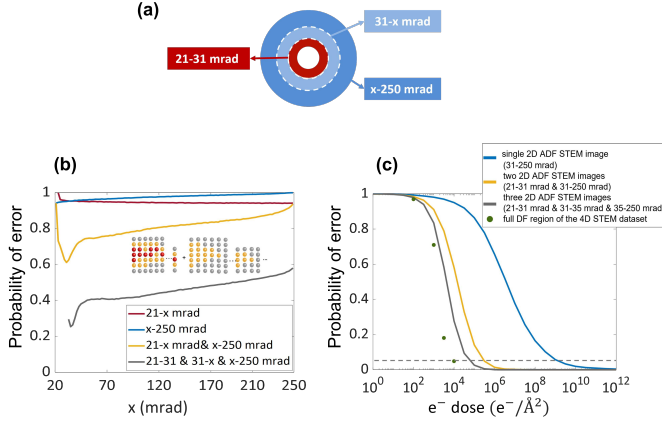


Figure 11: **Al@Au@Ag** - (a) annular subdivision of detector collection regime. (b) Probability of error as a function of the outer angle of a single ADF detector with fixed inner angle (red), the inner angle of a single ADF detector with fixed outer angle (blue), the common angle x for two independent detectors (yellow) and the common angle y for two independent detectors while the third detector has fixed settings (grey) for an incident electron dose of $10^4 e^-/\text{\AA}^2$. (c) Probability of error as a function of the incident electron dose calculated for a single ADF detector (blue), two independent ADF detectors (yellow), three independent ADF detectors (grey), and for the full dark field region of the 4D STEM dataset (green dots).

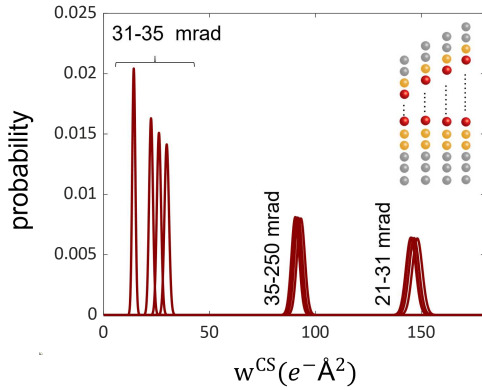


Figure 12: **Al@Au@Ag** - Probability functions for the selected hypotheses for an incident electron dose of $10^4 e^-/\text{\AA}^2$ based on the scattering cross-sections obtained from the three independent detectors.

Although the exact optimal detector angles depend on the selected examples, some standard practices could be derived from our study. For a single detector, the high amount of signal collected at the low angle ADF regime makes this region preferable. This is in agreement with findings from earlier studies [30, 40]. The availability of 4D STEM simulations enabled us now also to identify the optimal angles for the combination of two non-overlapping detector rings with the purpose of counting the number of atoms of two types of elements. Hereby, for the first detector, a narrow detector ring was found to be optimal with an inner angle just beyond the probe convergence angle, and the outer angle approximately 10 mrad larger than the inner angle. The largest improvement with the detector pair, as compared to the use of a single detector region, is observed for

mixed atomic columns with significantly different atomic numbers, as could be concluded for the pure and mixed Ag and Au atomic columns. When the differences in the scattering cross-sections are already very small for the single detector, such as for the depth location of an impurity atom or atoms with closely separated atomic numbers, the introduction of a second detector is not able to solve this complex problem at acceptable incident electron doses for atomic resolution imaging. Furthermore, we have shown that subdividing the annular detector region into three non-overlapping rings can significantly reduce the probability of error, when unscrambling more than two types of elements. This result also seem to suggest that the probability of error further decreases when using a multitude of ring detectors. Nevertheless, we expect the largest benefit from the subdivision into a limited number of detectors.

A great advantage of the here-applied approach is that, it enables us to investigate which electron dose is ultimately required to distinguish the different mixed atomic columns of a material under study with sufficient statistical significance. It should be noted that the probability of error reaches zero when the incident electron dose is increased. However, in an experimental study, some remaining errors might be present from effects which are not taken into account in this simulation study. These effects include e.g. beam damage, scan distortions, detector noise, amorphous layers on the surface, sample contamination, etc. When comparing from our study the probability of error as a function of dose for the scattering cross-sections of the optimal multiple detector regions and the full dark field region of the 4D STEM dataset, it is clear that employing the information of the full dark field region would further reduce the required electron dose. This reduction is most pronounced for determining the depth location of an impurity atom and unscrambling mixed element atomic columns with closely separated atomic numbers. In those cases, the 4D dataset provides significantly more information than the scattering cross-sections from multiple detector regions. However, the information available in the full dark field region of the 4D dataset is less accessible and more difficult to interpret than the scattering cross-sections from multiple detector regions.

In conclusion, we have shown that the concept of the probability of error can be used to find optimal strategies to count atoms from 4D STEM datasets. In particular, the method is generalised to create a set of multiple 2D STEM images providing independent information concerning thickness, composition, and ordering of the atoms along the viewing direction.

Acknowledgements

This work was supported by the European Research Council (Grant 770887 PICOMETRICS to S. Van Aert and Grant 823717 ESTEEM3). The authors acknowledge financial support from the Research Foundation Flanders (FWO, Belgium) through project fundings (G.0346.21N and EOS 30489208) and a postdoctoral grant to A. De Backer. S. Van Aert acknowledges funding from the University of Antwerp Research fund (BOF).

References

- [1] K. W. Urban, Studying Atomic Structures by Aberration-Corrected Transmission Electron Microscopy, *Science* 321 (2008) 506–510.
- [2] P. D. Nellist, S. J. Pennycook, The Principles and Interpretation of Annular Dark-Field Z-Contrast Imaging, *Advances in Imaging and Electron Physics* 113 (2000) 147–203.
- [3] A. J. den Dekker, S. Van Aert, A. van den Bos, D. Van Dyck, Maximum likelihood estimation of structure parameters from high resolution electron microscopy images. Part I: A theoretical framework, *Ultramicroscopy* 104 (2005) 83–106.
- [4] S. Van Aert, A. J. den Dekker, A. van den Bos, D. Van Dyck, J. H. Chen, Maximum likelihood estimation of structure parameters from high resolution electron microscopy images: Part II: A practical example, *Ultramicroscopy* 104 (2005) 107–125.
- [5] A. J. den Dekker, J. Gonnissen, A. De Backer, J. Sijbers, S. Van Aert, Estimation of unknown structure parameters from high-resolution (S)TEM images: What are the limits?, *Ultramicroscopy* 134 (2013) 34–43.
- [6] A. De Backer, K. H. W. van den Bos, W. Van den Broek, J. Sijbers, S. Van Aert, StatSTEM: An efficient approach for accurate and precise model-based quantification of atomic resolution electron microscopy images, *Ultramicroscopy* 171 (2016) 104–116.
- [7] R. Erni, H. Heinrich, G. Kostorz, Quantitative characterisation of chemical inhomogeneities in Al-Ag using high-resolution Z-contrast STEM, *Ultramicroscopy* 94 (2003) 125–133.
- [8] J. M. LeBeau, S. D. Findlay, L. J. Allen, S. Stemmer, Standardless Atom Counting in Scanning Transmission Electron Microscopy, *Nano Letters* 10 (2010) 4405–4408.
- [9] S. Van Aert, A. De Backer, G. T. Martinez, B. Goris, S. Bals, G. Van Tendeloo, Procedure to count atoms with trustworthy single-atom sensitivity, *Physical Review B* 87 (2013) 064107.
- [10] H. E. K. E. MacArthur, T. J. Pennycook, E. Okunishi, A. J. D’Alfonso, N. R. Lugg, L. J. Allen, P. D. Nellist, Probe integrated scattering cross sections in the analysis of atomic resolution HAADF STEM images, *Ultramicroscopy* 133 (2013) 109–119.
- [11] S. Van Aert, J. Verbeeck, R. Erni, S. Bals, M. Luysberg, D. Van Dyck, G. Van Tendeloo, Quantitative atomic resolution mapping using high-angle annular dark field scanning transmission electron microscopy, *Ultramicroscopy* 109 (2009) 1236–1244.
- [12] G. T. Martinez, A. De Backer, A. Rosenauer, J. Verbeeck, S. Van Aert, The effect of probe inaccuracies on the quantitative model-based analysis of high angle annular dark field scanning transmission electron microscopy images, *Micron* 63 (2014) 57–63.
- [13] K. E. MacArthur, A. J. D’Alfonso, D. Ozkaya, L. J. Allen, P. D. Nellist, Optimal ADF STEM imaging parameters for tilt-robust image quantification, *Ultramicroscopy* 156 (2015) 1–8.
- [14] A. De Backer, G. T. Martinez, A. Rosenauer, S. Van Aert, Atom counting in HAADF STEM using a statistical model-based approach: methodology, possibilities, and inherent limitations, *Ultramicroscopy* 134 (2013) 23–33.
- [15] L. Jones, K. E. MacArthur, V. T. Fauske, A. T. J. van Helvoort, P. D. Nellist, Rapid Estimation of Catalyst Nanoparticle Morphology and Atomic Coordination by High-Resolution Z-Contrast Electron Microscopy, *Nano Letters* 14 (2014) 6336–6341.
- [16] S. Van Aert, K. J. Batenburg, M. D. Rossell, R. Erni, G. Van Tendeloo, Three-dimensional atomic imaging of crystalline nanoparticles, *Nature* 470 (2011) 374–377.
- [17] G. T. Martinez, A. Rosenauer, A. De Backer, J. Verbeeck, S. Van Aert, Quantitative composition determination at the atomic level using model-based high-angle annular dark field scanning transmission electron microscopy, *Ultramicroscopy* 137 (2014) 12–19.
- [18] H. Akamine, K. H. W. van den Bos, N. Gauquelin, S. Farjami, S. Van Aert, D. Schryvers, M. Nishida, Determination of the atomic width of an APB in ordered CoPt using quantified HAADF-STEM, *Journal of Alloys and Compounds* 644 (2015) 570–574.
- [19] K. H. W. van den Bos, A. De Backer, G. T. Martinez, N. Winckelmans, S. Bals, P. D. Nellist, S. Van Aert, Unscrambling mixed elements using high angle annular dark field scanning transmission electron microscopy, *Physical Review Letters* 116 (2016) 246101.
- [20] C. Ophus, Four-Dimensional Scanning Transmission Electron Microscopy (4d-stem): From Scanning Nanodiffraction to Ptychography and Beyond, *Microscopy and Microanalysis* 25 (2019) 563–582.
- [21] A. R. Faruqi, G. McMullan, Direct imaging detectors for electron microscopy, *Nuclear Instruments & Methods in Physics Research, Section A: Accelerators, Spectrometers, Detectors, and Associated Equipment* 878 (2018) 180–190.
- [22] N. Shibata, Y. Kohno, S. D. Findlay, H. Sawada, Y. Kondo, Y. Ikuhara, New area detector for atomic-resolution scanning transmission electron microscopy, *Journal of Electron Microscopy* 59 (2010) 473–479.
- [23] Z. Chen, M. Weyland, P. Ercius, J. Ciston, C. Zheng, M. S. Fuhrer, A. J. D’Alfonso, L. J. Allen, S. D. Findlay, Practical aspects of diffractive imaging using an atomic-scale coherent electron probe, *Ultramicroscopy* 169 (2016) 107–121.
- [24] H. Yang, R. N. Rutte, L. Jones, M. Simson, R. Sagawa, H. Ryll, M. Huth, S. J. Pennycook, M. L. H. Green, H. Soltau, Y. Kondo, B. G. Davis, P. D. Nellist, Simultaneous atomic-resolution electron ptychography and Z-contrast imaging of light and heavy elements in complex nanostructures, *Nature Communications* 7 (2016) 2532.
- [25] Y. Wen, C. Ophus, C. S. Allen, S. Fang, J. Chen, E. Kaxiras, A. I. Kirkland, J. H. Warner, Simultaneous Identification of Low and High Atomic Number Atoms in Monolayer 2D Materials Using 4D Scanning Transmission Electron Microscopy, *Nano Letters* 19 (2019) 6482–6491.
- [26] K. Müller-Caspary, O. Oppermann, T. Grieb, F. F. Krause, A. Rosenauer, M. Schowalter, T. Mehrtnes, A. Beyer, K. Volz, P. Potapov, Materials characterisation by angle-resolved scanning transmission electron microscopy, *Scientific Reports* 6 (2016) 37146.
- [27] J. Y. Zhang, J. Hwang, B. J. Isaac, S. Stemmer, Variable-angle high-angle annular dark-field imaging : application to three-dimensional dopant atom profiling, *Scientific Reports* 5 (2015) 12419.
- [28] N. Winckelmans, T. Altantzis, M. Grzelczak, A. Sánchez-Iglesias, L. Liz-Marzán, S. Bals, Multimode electron tomography as a tool to characterize the internal structure and morphology of gold nanoparticles, *The Journal of Physical Chemistry C* 122 (2018) 13522–13528.
- [29] J. Gonnissen, A. De Backer, A. J. den Dekker, G. T. Martinez, A. Rosenauer, J. Sijbers, S. Van Aert, Optimal experimental design for the detection of light atoms from high-resolution scanning transmission electron microscopy images, *Applied Physics Letters* 105 (2014) 063116.
- [30] A. De Backer, A. De wael, J. Gonnissen, S. Van Aert, Optimal experimental design for nano-particle atom-counting from high-resolution STEM images, *Ultramicroscopy* 151 (2015) 46–55.
- [31] A. M. Mood, F. A. Graybill, D. C. Boes, Introduction to the Theory of Statistics, 3 ed., McGraw-Hill Book Company, 1974.
- [32] I. Lobato, D. Van Dyck, MULTTEM: A new multislice program to perform accurate and fast electron diffraction and imaging simulation using Graphics Processing Units with CUDA, *Ultramicroscopy* 156 (2015) 9–17.
- [33] A. Beyer, F. F. Krause, H. L. Robert, S. Firoozabadi, T. Grieb, P. Kükelhan, D. Heimes, M. Schowalter, K. Müller-Caspary, A. Rosenauer, K. Volz, Influence of plasmon excitations on atomic-resolution quantitative 4d scanning transmission electron microscopy, *Sci Rep* 10 (2020) 17890.
- [34] A. P. Thompson, H. M. Aktulga, R. Berger, D. S. Bolintineanu, W. M. Brown, P. S. Crozier, P. J. in ’t Veld, A. Kohlmeyer, S. G. Moore, T. D. Nguyen, R. Shan, M. J. Stevens, J. Tranchida, C. Trott, S. J. Plimpton, LAMMPS - a flexible simulation tool for particle-based materials modeling at the atomic, meso, and continuum scales, *Computer Physics Communications* 271 (2022) 108171.
- [35] S. Plimpton, Fast Parallel Algorithms for Short-Range Molecular Dynamics, *Journal of Computational Physics* 117 (1995) 1–19.
- [36] K. W. Jacobsen, P. Stoltze, J. K. Nørskov, A semi-empirical effective medium theory for metals and alloys, *Surface Science* 366 (1996) 394–402.
- [37] K. H. W. van den Bos, L. Janssens, A. De Backer, P. D. Nellist, S. Van Aert, The atomic lensing model: New opportunities for atom-by-atom metrology of heterogeneous nanomaterials, *Ultramicroscopy* 203 (2019) 155–162.
- [38] J. W. M. Crawley, I. e. Gow, N. Lawes, I. Kowalec, L. Kabalan, C. R. A. Catlow, A. J. Logsdail, S. H. Taylor, N. F. Dummer, G. J. Hutchings, Heterogeneous Trimetallic Nanoparticles as Catalysts, *Chemical Reviews* 122 (2022) 6795–6849.
- [39] H. Kim, T. Y. Yoo, M. S. Bootharaju, J. H. Kim, D. Y. Chung, T. Hyeon, Noble Metal-Based Multimetallic Nanoparticles for Electrocatalytic Applications, *Advanced Science* 9 (2022) 2104054.

- [40] R. Hovden, D. A. Muller, Efficient elastic imaging of single atoms on ultrathin supports in a scanning transmission electron microscope, *Ultramicroscopy* 123 (2012) 59–65.